International Journal of Power Electronics and Drive System (IJPEDS)
Vol. 17, No. 4, December 2026, pp. 2403~2412
ISSN: 2088-8694, DOI: 10.11591/ijpeds.v17.i4.pp2403-2412

Comparison of multicarrier PWM switching techniques for cascaded H-bridge induction motor drives

Nattapong Pothi, Buntueng Yana, Jonglak Pahasa, Chawasak Rakpenthai
Department of Electrical Engineering, School of Engineering, University of Phayao, Phayao, Thailand

Article Info

Article history:

Received Apr 7, 2026
Revised Aug 23, 2026
Accepted Sep 17, 2026

Keywords:

Cascade H-bridge
Induction motor
Multilevel inverter
Switching techniques
Torque ripple

ABSTRACT

This article proposes a comparative study of multicarrier switching techniques for 5-level cascaded H-bridge (CHB) induction motor drives, with emphasis on the impact of torque ripple. Phase-shifted (PS) and level-shifted (LVS) techniques are typically applied in multilevel inverters. Likewise, the LVS technique can be classified into three categories based on the arrangement of the carrier signals, including alternate phase opposition disposition (APOD), phase opposition disposition (POD), and in-phase opposition disposition (IPD). A 5-level CHB inverter can provide fault tolerance, operate with low-voltage sources, and reduce torque ripple; nonetheless, selecting switching techniques is crucial, as they can significantly influence drive performance. Hence, all switching techniques are verified under no-load and loaded conditions over the entire speed range, considering total harmonic distortion, torque ripple, and copper loss. Simulation results validate the performance of the 5-level CHB induction motor drive under multicarrier switching techniques.

This is an open access article under the CC BY-SA license.

Corresponding Author:

Buntueng Yana
Department of Electrical Engineering, School of Engineering, University of Phayao
19 Moo.2, Meaka, Muang Phayao, Phayao 56000, Thailand
Email: buntueng.ya@up.ac.th

1. INTRODUCTION

Induction motors (IMs) are widely applied across various industrial sectors owing to their robustness and low maintenance requirements compared to other motor types [1]. These motors may deliver power from several hundred watts to several megawatts for drive systems [2]. Moreover, high-precision speed control and rapid dynamic response are required in specific applications, e.g., high-speed conveyors, pumps, electric vehicles (EVs), and military equipment; hence, a variable-speed drive with numerous high-performance vector control methods is proposed [3]. Nevertheless, torque ripple is a critical issue that can affect the performance of the drive system, as it refers to the periodic variation in output torque instead of a constant value, resulting in mechanical vibration, acoustic noise, and decreased precision [4]. Although field-oriented control (FOC) is frequently employed with a two-level voltage source inverter (VSI) in various motor drive applications because of its inherent ability to reduce the torque ripple compared to the direct torque control (DTC) method [5], the total harmonic distortion (THD) and inverter loss caused by high switching frequency are still the main points that should be addressed. Therefore, several methods have been proposed, including control- and design-based approaches, to solve the aforementioned problems. In [6]-[8], a model-based predictive control is proposed to minimize the torque ripple and enhance the efficiency. A robustness control against thermal variations in the rotor to reduce the cause of torque instability is presented in [9]. Meanwhile, an artificial neural network is used to estimate the rotor speed and flux to achieve low torque ripple, especially at the low speed reported in [10]. However, these control approaches may be

difficult to implement due to their high computational burden, limiting their practical application. Furthermore, a two-level VSI is employed in the mentioned methods, which can still affect drive system performance due to high THD and inverter losses. In contrast, a multilevel inverter can reduce these effects, making it a preferable option for high-precision motor drive applications [11].

Cascade H-bridge (CHB) multilevel inverters have become significant in medium-voltage and high-power motor drive systems owing to their minimal harmonic distortion, fault tolerance, modular architecture, and ability to generate high-quality output voltage waveforms [12], [13]. Additionally, the switching frequency in the CHB multilevel inverter is typically lower than that of a conventional two-level VSI, resulting in a significant reduction in switching losses [14]-[16]. The CHB multilevel inverter efficiently utilizes low-voltage sources to generate a high output voltage, which is especially beneficial in applications that rely on low-voltage sources, such as photovoltaic power systems. The CHB multilevel inverter is widely used in IM drives across several sectors due to its advantages [17], which are important for EV and hybrid EV applications. Researchers have also compared the harmonic performance, semiconductor losses, and modularity of CHB topologies with other multilevel structures and single-DC-source configurations [18], [19]. Nonetheless, reducing torque ripple and speed variations remains a focus [20].

Multicarrier pulse-width modulation (PWM) used to generate pulses for the CHB multilevel inverter is classified into two categories, including phase-shifted (PS) and level-shifted (LVS). The LVS approach can also be categorized into three types based on the arrangement of the carrier signals: alternative phase opposition disposition (APOD), phase opposition disposition (POD), and in-phase opposition disposition (IPD) [21]. However, the selection of the multicarrier PWM switching techniques can directly and significantly affect drive system performance and torque ripple [22], which is a critical aspect to consider.

Unlike prior comparative studies that evaluate multicarrier PWM switching techniques under open-loop conditions without closed-loop drive control [22], this paper standardizes the average device switching frequency across all techniques [23] and evaluates their impact within a closed-loop FOC with a 5-level CHB IM drive. This paper compares PS and LVS strategies, including APOD, POD, and IPD, with an emphasis on their effects on drive system performance and torque ripple. All switching techniques are verified under no-load and loaded conditions over the entire speed range, jointly considering total harmonic distortion, torque ripple, and copper loss, as confirmed by simulation results.

2. CASCADE H-BRIDGE MULTILEVEL INVERTER

2.1. CHB configuration

The CHB multilevel inverter is a modular arrangement of isolated H-bridge cells, each powered by a separate DC source. All H-bridge cells in each phase are connected in series, as shown in Figure 1, indicating a 5-level CHB inverter. Accordingly, the output voltage can be increased in direct proportion to the number of voltage levels, corresponding to the total number of H-bridge cells, as given by (1). Likewise, the total number of switches employed in the CHB multilevel inverter can be determined using (2) [24]. Although the CHB inverter requires numerous separate DC sources, it offers fault tolerance and efficiently utilizes low-voltage sources to generate a higher output voltage, which is particularly beneficial in many applications [25]:

$$m = 2H + 1 \tag{1}$$

$$N_{SW} = 6(m - 1) \tag{2}$$

where m denotes the number of voltage levels, H means the total number of H-bridge cells in each phase, and N_{SW} is the total number of operating switches.

2.2. Multicarrier switching techniques

In a cascaded H-bridge multilevel inverter, the objective of multicarrier switching is to coordinate the triggering pulses of several H-bridge cells to achieve a high-quality cascade output voltage. Accordingly, THD can be significantly reduced compared to the conventional two-level inverter, thereby enhancing drive system performance. Besides, there are two primary categories of multicarrier switching techniques: PS and LVS, which comprise APOD, POD, and IPD. Figure 2 illustrates the generation of PWM signals for all switching techniques. In Figure 2(a), the modulation signal (Ta) is compared with triangular carrier signals on both the positive and negative sides (Vcrx+, Vcrx-), as given in (3) and (4), respectively, to generate pulses that switch the H-bridge cell. The number of triangular carrier signals is determined by the voltage levels of the CHB inverter, specifically (m-1); hence, there are 4 triangular carrier signals for the 5-level CHB inverter. The positive side of the triangular carrier signals is employed for SA11 and SA21, which are the front legs of the H-bridge cells. In contrast, the negative side of the triangular carrier signals is employed for SA23 and SA13, which are the same sequence as the triangular carrier signal. Indeed, switches on the same leg cannot be

triggered simultaneously, e.g., SA11 and SA12, because they are interlocked; hence, the NOT gate is used, as shown in Figure 2(a). The triggered pulse signals for the phase-shifted and level-shifted techniques, which differ significantly in the triangular carrier signal arrangement, are illustrated in Figures 2(b)-2(e), respectively:

$$S_{A11,A21} = \begin{cases} 1 & ; \quad T_a \geq V_{crx+} \\ 0 & ; \quad T_a < V_{crx+} \end{cases} \tag{3}$$

$$S_{A23,A13} = \begin{cases} 1 & ; \quad T_a \leq V_{crx-} \\ 0 & ; \quad T_a > V_{crx-} \end{cases} \tag{4}$$

where T_a means the modulation signal of phase A, V_{crx+}, V_{crx-} are triangular carrier signals on the positive and negative sides, respectively, and x denotes a sequence number (x = 1, 2).

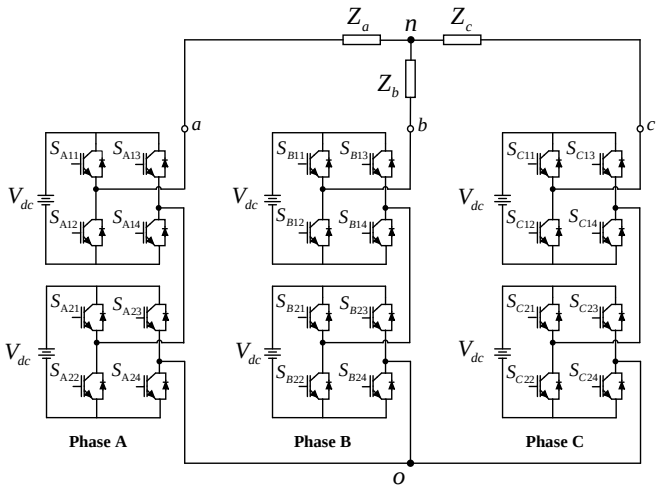

Figure 1. 5-level CHB inverter

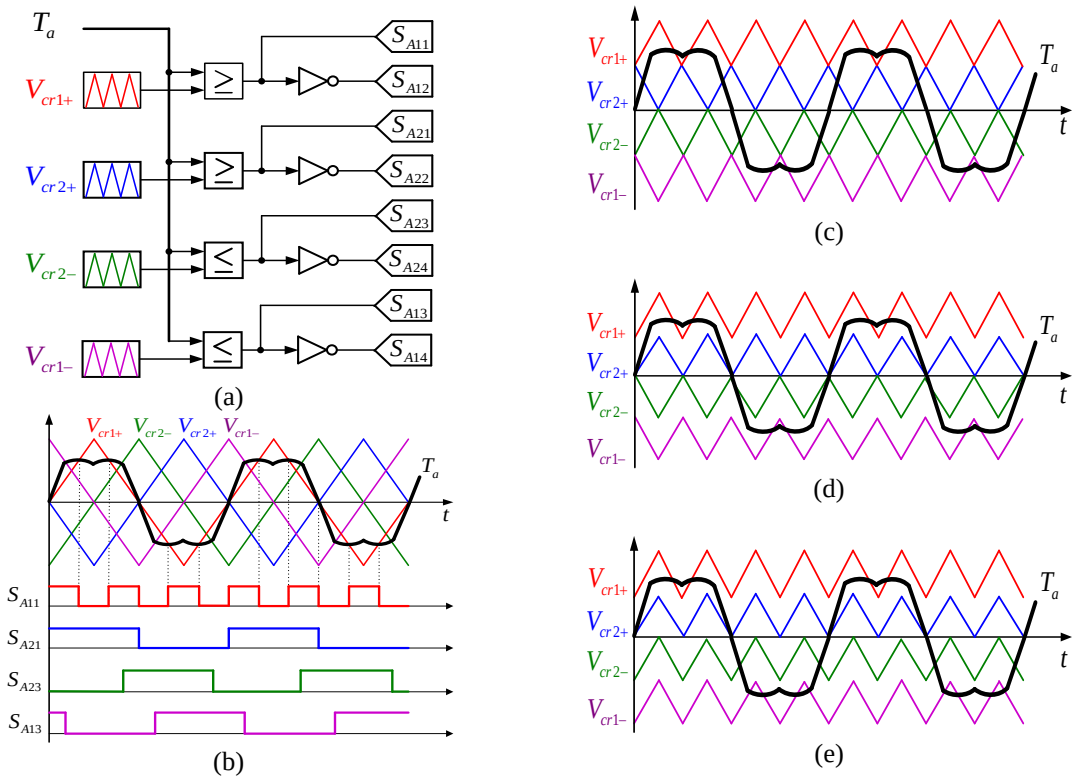

Figure 2. Multicarrier switching techniques for 5-level CHB of phase A: (a) PWM signal generation, (b) PS, (c) APOD, (d) POD, and (e) IPD techniques

3. CHB IM DRIVES

The indirect rotor flux-oriented control of the 5-level CHB IM drive is shown in Figure 3. Under this approach, the rotor flux linkage is regulated by the d-axis current, independently of torque, which is controlled by the q-axis current [26]. The d-axis reference current is typically configured to align with the designed rotor flux, which is usually specified on the motor's nameplate and can be determined by (5). Meanwhile, the q-axis reference current is governed by the speed control loop, which is calibrated to satisfy the torque requirement, as indicated in Figure 3. Although the FOC strategy requires at least three regulators for both the current and speed control loops, which depend on motor parameters, it provides low acoustic noise and low torque ripple:

$$i_{ds}^{*} = \frac{\psi_{dr}}{L_m} \tag{5}$$

where * indicates the reference value, ψ_{dr} is the rotor flux on the *d*-axis, and L_m is the mutual inductance.

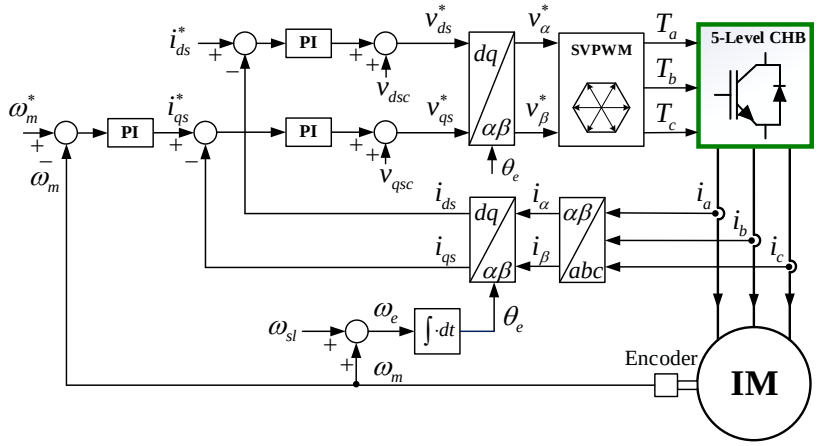

Figure 3. FOC control diagram of the 5-level CHB IM drives

An electrical angular position is primarily used in the transformation process under the FOC strategy. It can be determined by the combination of the measured mechanical angular speed and the slip angular speed, as given in (6). The slip angular speed can be determined from motor parameters and currents, as given by (7). The electrical angular position is crucial for the drive system performance, as it enables precise conversion of armature currents into the *d-q* axes aligned with the synchronous reference frame. Therefore, the orthogonality of the controlled currents provides separate control of rotor flux and torque [27]:

$$\theta_e = \int (\omega_{sl} + \omega_r)\, dt = \int \omega_e\, dt \tag{6}$$

$$\omega_{sl} = \frac{R_r}{L_r} \frac{i_{qs}}{i_{ds}} \tag{7}$$

where θ_e denotes an electrical angular position, and ω_{sl} means the slip angular speed in rad/s.

4. SIMULATION RESULTS VERIFICATION

A 4.3 kW three-phase squirrel cage induction motor with a line voltage of 304 V is employed to verify the switching techniques. The motor parameters and control settings are indicated in Table 1. The 5-level CHB IM drive based on the FOC strategy is simulated in MATLAB/Simulink. The model is solved by using the variable-step ODE45 (Dormand-Prince) solver with the step size automatically adjusted according to a relative tolerance of 1e-6. The PWM gating signals are generated by naturally sampled comparison of symmetrical triangle carrier signals against the continuous modulation signal obtained from the SVPWM, consistent with the comparison logic in (3) and (4). The 5-level configuration (H=2) is adopted as the minimum CHB structure corresponding to (1), with the APOD, POD, and IPD carrier arrangements producing distinguishable switching patterns while remaining representative of low-voltage source CHB applications as mentioned in section 1. The 200 rpm and 1,000 rpm operating points are selected to verify performance across the practical speed range: 200 rpm represents a low-speed, low-modulation-index

condition where torque ripple is typically most severe, while 1,000 rpm, nearly 68.96% of the 1,450-rpm base speed, denotes a near base-speed condition for comparison. The d-axis current reference is defined at 6.3 A, corresponding to the d-axis rotor flux as given by (5). Likewise, the DC-link voltage in each H-bridge cell is set to 75.0 V, which is sufficient to achieve the motor's base speed. Indeed, the average device switching frequency of the LVS technique equals the carrier switching frequency, whereas that of the PS technique is given by (8) [23]. Therefore, this study assumes the average device switching frequency across all verified switching techniques is equal, with the PS technique set to 500 Hz, as shown in Table 1:

$$f_{s,PS} = \frac{f_s}{(m-1)} \tag{8}$$

where $f_{s,PS}$ denotes the average device switching frequency of the PS technique.

Table 1. Motor parameters and control settings

Motor parameters	Symbols	Values	Control setting	Symbols	Values
Base speed	ω_{base}	1,450 rpm	Maximum current	I_m	12.0 A
Pole pairs	p	2	DC-link voltage	V_{dc}	75.0 V
Stator resistance	R_s	0.711 Ω	Carrier switching frequency	f_s	2,000 Hz
Rotor resistance	R_r	0.441 Ω	Switching frequency of the PS	$f_{s,PS}$	500 Hz
Stator leakage inductance	L_{ls}	0.003209 H	Bandwidth of the current control loop	ω_{bc}	2827.433 rad/s
Rotor leakage inductance	L_{lr}	0.004594 H	Bandwidth of the speed control loop	ω_{bs}	282.743 rad/s
Mutual inductance	L_m	0.06978 H	PI regulator gains of the d-q axis	$k_{pc,d}$, $k_{pc,q}$	28.9672
Rotor flux on d-axis	ψ_{dr}	0.445 Wb	current control loops	$k_{ic,d}$, $k_{ic,q}$	6112
Moment of inertia	J	0.0138 kg m^2	PI regulator gains of the speed control	k_{ps}	5.5176
Friction coefficient	B	0.000503 Nm/s	loop	k_{is}	1103.2

Figure 4 shows the voltage and current waveforms for the 5-level CHB IM drive operating at 200 rpm with a load torque of 10.0 Nm, which compares the results of the PS, APOD, POD, and IPD techniques. It is clear that the voltage and current waveforms for the PS, APOD, and POD techniques are almost identical, as shown in Figures 4(a)-4(c), whereas the IPD technique exhibits the lowest current ripple, as expressed in Figure 4(d). Likewise, the IPD technique shows the same trend at 1,000 rpm, as shown in Figure 5. Besides, the line-voltage magnitude of the IPD technique is lower than that of other techniques owing to a distinct modulation signal caused by lower current ripple, as shown in Figure 6.

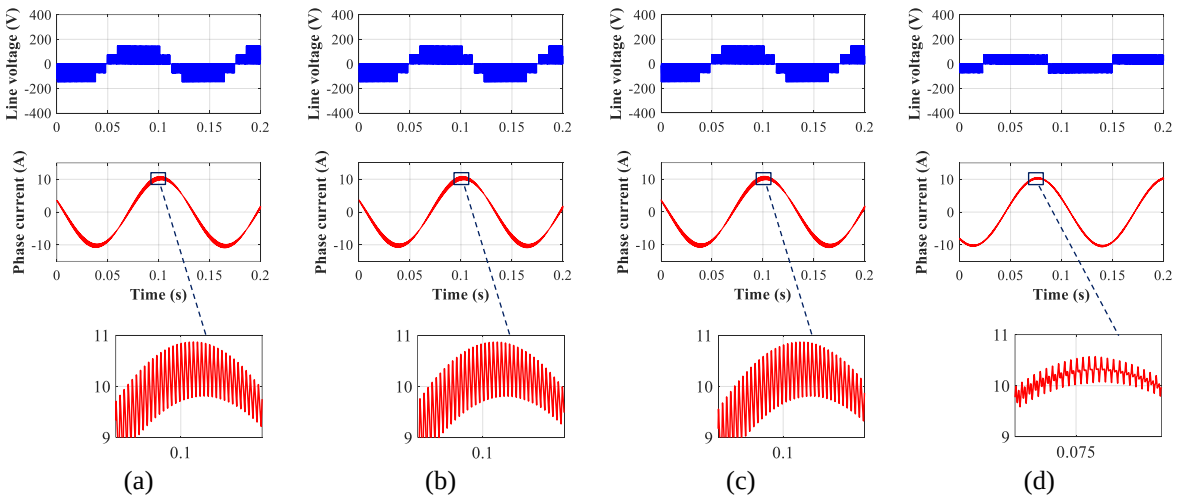

Figure 4. Voltage and current waveforms at 200 rpm: (a) PS, (b) APOD, (c) POD, and (d) IPD techniques

Figure 6 illustrates the effective tracking performance of the d-axis and q-axis currents, as well as the modulation signal performed with all switching techniques. The speed is initially set at 200 rpm and increased to 1,000 rpm at 0.3 seconds while maintaining a constant load torque of 10.0 Nm. It is evident that a higher current ripple in the PS, APOD, and POD results in a higher modulation signal, as expressed in Figure 6(a)-

6(c), which changes the voltage waveform. The results indicate that the IPD technique produces the lowest current ripple and delivers a rapid dynamic response, enabling it to reach 1,000 rpm faster than others, but a slight overshoot has emerged, as shown in Figure 6(d). Furthermore, Figure 7 illustrates THD performance at various speeds with a load torque of 10.0 Nm, demonstrating that the IPD exhibits superior performance across all speed ranges in both voltage and current. It is noted that higher speed correlates with lower THD. The superior performance of IPD arises from its carrier arrangement, in which all carrier signals share the same phase, as shown in Figure 2(e), so the dominant switching frequency harmonics generated by each carrier band coincide and partially cancel in the resulting line-to-line voltage [21]. In contrast, APOD and POD introduce phase offsets between adjacent carrier bands, spreading harmonic energy across a wider sideband and increasing current ripple. Since the current controllers on the *d*- and *q*-axis respond to this current ripple, the resulting modulation signal in APOD and POD exhibits larger fluctuations, as shown in Figures 6(a)-6(c), which propagate into higher torque ripple through the induced torque's dependence on the *q*-axis current.

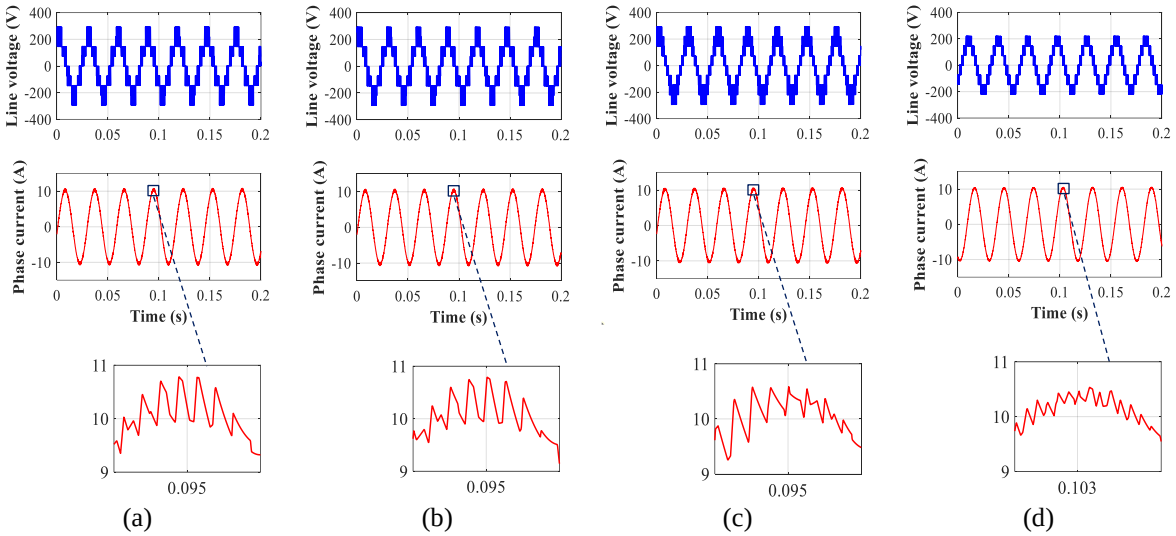

Figure 5. Voltage and current waveforms at 1,000 rpm: (a) PS, (b) APOD, (c) POD, and (d) IPD techniques

The effects of the current ripple on torque for all switching techniques, under both no-load and loaded conditions (10.0 Nm), starting at 0.3 seconds, are shown in Figure 8. The IPD technique consistently exhibits the lowest torque ripple under loaded conditions, with a value of 1.244 percent at 200 rpm, while other methods are 4.459 percent, as shown in Figure 8(a). Likewise, the IPD torque ripple is 1.021 percent at 1,000 rpm, while the torque ripple of the PS and APOD methods is 2.193 percent and 2.864 percent for the POD, as indicated in Figure 8(b). Compared to APOD and POD, the IPD technique can reduce torque ripple by approximately 72.1% (from 4.459% to 1.244%) at 200 rpm and by 54.5-64.3% (from 2.193% and 2.864% to 1.021%) at 1,000 rpm. It is observed that the torque ripple increases in the low-speed region (200 rpm) and decreases in the high-speed region (1,000 rpm), corresponding to the current ripple and THD, as shown in Figures 6 and 7, respectively. In addition, a high torque ripple is clearly observed under loaded conditions rather than under no-load conditions. However, the IPD technique exhibits torque overshoot when the load is applied at 0.3 seconds, matching the current response, as shown in Figure 6. This overshoot is quantified as follows: in the *q*-axis current response, PS, APOD, and POD exhibit an overshoot of around 12.42%, whereas IPD is around 29.93%. The same trend appears in the induced torque response, as shown in Figure 8: at 200 rpm, PS, APOD, and POD exhibit a torque overshoot of about 28.895%, compared to approximately 46.335% for IPD. Meanwhile, at 1,000 rpm, PS, APOD, and POD show about 27.905% torque overshoot, compared to around 59.439% for IPD. This result is attributed to IPD's lower steady-state current ripple, which lets the current controller track the reference more aggressively during transients, producing a faster but less damped response. It also represents a compromise between steady-state ripple performance and transient overshoot that should be considered in some applications sensitive to torque transients, such as EV traction drives during rapid acceleration demands. Furthermore, the current ripple not only affects the torque ripple but can also increase the copper loss of the 5-level CHB IM drive, as shown in Figure 9.

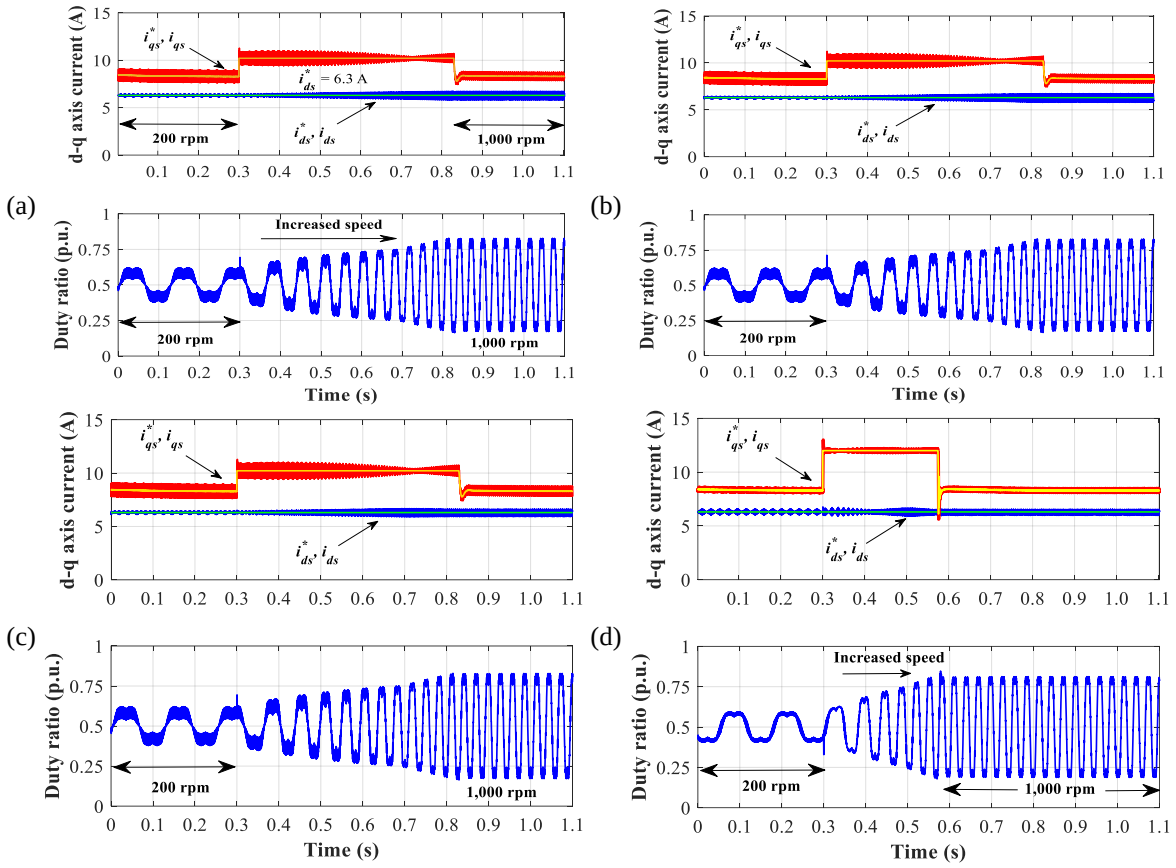

Figure 6. *d-q* axis current and modulation signal: (a) PS, (b) APOD, (c) POD, and (d) IPD techniques

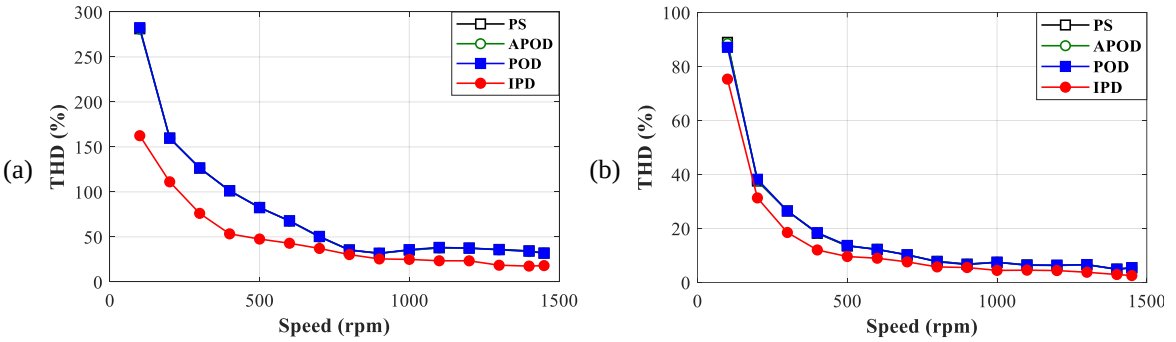

Figure 7. Total harmonic distortion: (a) line voltage and (b) phase current

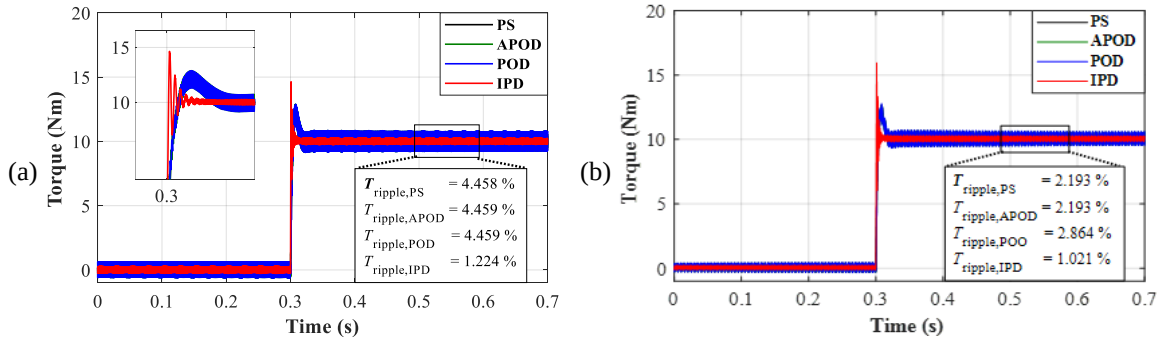

Figure 8. Induced torque in no-load and loaded conditions: (a) 200 rpm and (b) 1,000 rpm

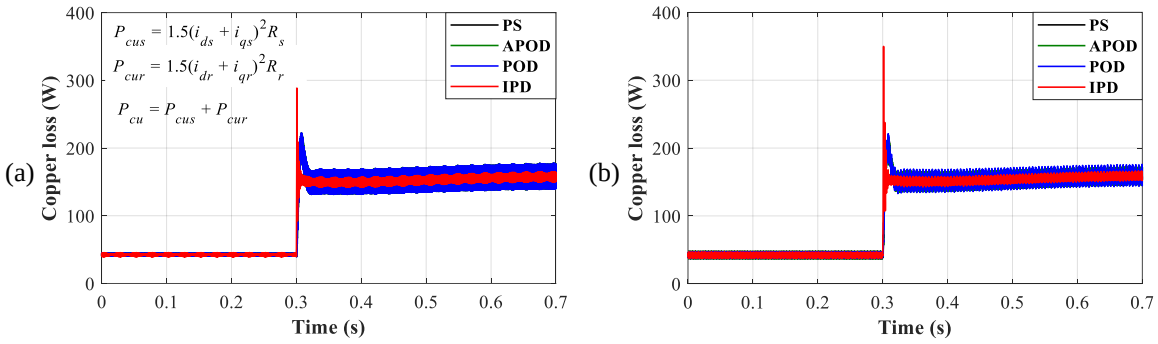

Figure 9. Copper loss in no-load and loaded conditions: (a) 200 rpm and (b) 1,000 rpm

5. CONCLUSION

The multicarrier PWM switching methods for the 5-level CHB IM drives, in both phase-shifted (PS) and level-shifted techniques, including APOD, POD, and IPD, have been verified and compared in terms of drive performance, with a focus on torque ripple. The results demonstrate that the IPD technique produces the lowest current ripple among the other switching techniques, resulting in the least torque ripple. Under the FOC strategy, the IPD also provides the lowest THD for both current and voltage waveforms across all speed ranges and exhibits a faster dynamic response than others. Higher speeds correlate with decreased current ripple, THD, and torque ripple. Furthermore, the current ripple not only influences the torque ripple but may also increase the copper loss in the CHB IM drive. These findings are particularly relevant to EV and hybrid-EV traction drives and photovoltaic-fed motor drive systems, in which low-voltage CHB configurations are typically utilized, and torque ripple directly affects ride comfort and mechanical stress. This study is limited to simulation-based verification; experimental validation on a hardware CHB prototype is required to confirm these results under actual component non-idealities, such as dead time and DC-link voltage imbalance. For the transient overshoot observed for IPD, future work will explore adaptive or hybrid switching strategies that combine IPD's low-ripple steady-state behavior with improved transient damping.

FUNDING INFORMATION

This research was supported by the University of Phayao and the Thailand Science Research and Innovation Fund 2025.

AUTHOR CONTRIBUTIONS STATEMENT

This journal uses the Contributor Roles Taxonomy (CRediT) to recognize individual author contributions, reduce authorship disputes, and facilitate collaboration.

Name of Author	C	M	So	Va	Fo	I	R	D	O	E	Vi	Su	P	Fu
Nattapong Pothi	✓	✓	✓	✓	✓	✓	✓	✓	✓	✓	✓		✓	✓
Buntueng Yana				✓	✓	✓		✓	✓	✓				✓
Jonglak Pahasa				✓		✓				✓		✓		
Chawasak Rakpenthai	✓			✓		✓				✓		✓		

C : **C**onceptualization
M : **M**ethodology
So : **So**ftware
Va : **Va**lidation
Fo : **Fo**rmal analysis
I : **I**nvestigation
R : **R**esources
D : **D**ata Curation
O : Writing - **O**riginal Draft
E : Writing - Review & **E**diting
Vi : **Vi**sualization
Su : **Su**pervision
P : **P**roject administration
Fu : **Fu**nding acquisition

CONFLICT OF INTEREST STATEMENT

The authors declare that they have no known competing financial interests or personal relationships that could have appeared to influence the work reported in this paper.

DATA AVAILABILITY

The authors confirm that the data supporting the findings of this study are available within the article.

REFERENCES

[1] R. Hussain, M. Alshaikh Saleh, and S. S. Refaat, "Various faults classification of industrial application of induction motors using supervised machine learning: a comprehensive review," *IEEE Access*, vol. 13, pp. 146649–146675, 2025, doi: 10.1109/ACCESS.2025.3600570.

[2] K. Vostrov, L. Aarniovuori, and J. Pyrhonen, "High-speed megawatt-scale induction-motor drives: Efficiency maps and drivetrains," in *2022 International Conference on Electrical Machines (ICEM)*, Sep. 2022, pp. 745–751, doi: 10.1109/ICEM51905.2022.9910826.

[3] H. Gashtil, V. Pickert, D. J. Atkinson, M. Dahidah, and D. Giaouris, "Improved voltage boundary with model-based control algorithm for increased torque in the field weakening region of induction machines," *IEEE Transactions on Transportation Electrification*, vol. 7, no. 3, pp. 1600–1614, Sep. 2021, doi: 10.1109/TTE.2020.3048306.

[4] H.-J. Cho, Y.-C. Kwon, and S.-K. Sul, "Torque ripple-minimizing control of IPMSM with optimized current trajectory," *IEEE Transactions on Industry Applications*, vol. 57, no. 4, pp. 3852–3862, Jul. 2021, doi: 10.1109/TIA.2021.3075424.

[5] M. Bermúdez, F. Barrero, C. Martín, and M. Perales, "Performance analysis of direct torque controllers in five-phase electrical drives," *Applied Sciences*, vol. 11, no. 24, Dec. 2021, doi: 10.3390/app112411964.

[6] J. Kim, S.-W. Ryu, M. S. Rafaq, H. H. Choi, and J.-W. Jung, "Improved torque ripple minimization technique with enhanced efficiency for surface- mounted PMSM drives," *IEEE Access*, vol. 8, pp. 115017–115027, 2020, doi: 10.1109/ACCESS.2020.3004042.

[7] Y. Zhang, H. Yang, and B. Xia, "Model predictive torque control of induction motor drives with reduced torque ripple," *IET Electric Power Applications*, vol. 9, no. 9, pp. 595–604, Nov. 2015, doi: 10.1049/iet-epa.2015.0138.

[8] M. B. Hossen and M. Habibullah, "Robust model-free predictive torque control for induction motor drive based on an ultralocal model," *IEEE Access*, vol. 13, pp. 47514–47524, 2025, doi: 10.1109/ACCESS.2025.3550924.

[9] S. M. N. Ali *et al.*, "Robust sensorless control against thermally degraded speed performance in an IM drive based electric vehicle," *IEEE Transactions on Energy Conversion*, vol. 35, no. 2, pp. 896–907, Jun. 2020, doi: 10.1109/TEC.2020.2968547.

[10] S. Usha, C. Subramani, and S. Padmanaban, "Neural network-based model reference adaptive system for torque ripple reduction in sensorless poly phase induction motor drive," *Energies*, vol. 12, no. 5, Mar. 2019, doi: 10.3390/en12050920.

[11] Akshat, M. V. Naik, and R. Kumar, "Performance analysis of an induction motor drive powered by a cascaded H-bridge multilevel inverter," *Discover Electronics*, vol. 2, no. 1, Jun. 2025, doi: 10.1007/s44291-025-00081-y.

[12] Z. Ni, A. H. Abuelnaga, and M. Narimani, "A new fault-tolerant technique based on nonsymmetrical selective harmonic elimination for cascaded H-bridge motor drives," *IEEE Transactions on Industrial Electronics*, vol. 68, no. 6, pp. 4610–4622, Jun. 2021, doi: 10.1109/TIE.2020.2989705.

[13] H. Yao, Y. Yan, Y. Cao, P. Song, and T. Shi, "A variable duty cycle-based predictive control for PMSM fed by cascaded H-bridge inverter," *IEEE Journal of Emerging and Selected Topics in Power Electronics*, vol. 10, no. 4, pp. 4195–4206, Aug. 2022, doi: 10.1109/JESTPE.2022.3154045.

[14] P. S. Jamwal, S. Singh, and S. Jain, "Three-level inverters for induction motor driven electric vehicles," in *2020 3rd International Conference on Energy, Power and Environment: Towards Clean Energy Technologies*, Mar. 2021, pp. 1–6, doi: 10.1109/ICEPE50861.2021.9404444.

[15] N. Abd Rahim, M. Mohamad Elias, and W. Hew, "Transistor-clamped H-Bridge based cascaded multilevel inverter with new method of capacitor voltage balancing," *IEEE Transactions on Industrial Electronics*, vol. 60, no. 8, pp. 2943–2956, 2013, doi: 10.1109/TIE.2012.2200213.

[16] P. Kant and B. Singh, "Multiwinding transformer fed CHB inverter with on-line switching angle calculation based SHE technique for vector controlled induction motor drive," *IEEE Transactions on Industry Applications*, vol. 56, no. 3, pp. 2807–2815, May 2020, doi: 10.1109/TIA.2020.2980131.

[17] G. Pongnot, A. Desreveaux, C. Mayet, D. Labrousse, and F. Roy, "Comparative analysis of a low-voltage CHB inverter without PWM and two-level IGBT/SiC inverters for electric vehicles on driving cycles," *IEEE Open Journal of Vehicular Technology*, vol. 6, pp. 542–553, 2025, doi: 10.1109/OJVT.2025.3531652.

[18] J. Pereda and J. Dixon, "High-frequency link: a solution for using only one dc source in asymmetric cascaded multilevel inverters," *IEEE Transactions on Industrial Electronics*, vol. 58, no. 9, pp. 3884–3892, Sep. 2011, doi: 10.1109/TIE.2010.2103532.

[19] D. A. B. Zambra, C. Rech, and J. R. Pinheiro, "Comparison of neutral-point-clamped, symmetrical, and hybrid asymmetrical multilevel inverters," *IEEE Transactions on Industrial Electronics*, vol. 57, no. 7, pp. 2297–2306, Jul. 2010, doi: 10.1109/TIE.2010.2040561.

[20] M. A. Tariq and S. A. Rahman Kashif, "Impact of the voltage profiles of CHB vs MW-type inverters on torque and speed ripples for 3-phase induction motors," in *2024 IEEE Workshop on Control and Modeling for Power Electronics (COMPEL)*, Jun. 2024, pp. 1–7, doi: 10.1109/COMPEL57542.2024.10613975.

[21] B. P. McGrath and D. G. Holmes, "Multicarrier PWM strategies for multilevel inverters," *IEEE Transactions on Industrial Electronics*, vol. 49, no. 4, pp. 858–867, Aug. 2002, doi: 10.1109/TIE.2002.801073.

[22] A. S. R. A. Subki *et al.*, "Analysis on three phase cascaded H-bridge multilevel inverter based on sinusoidal and third harmonic injected pulse width modulation via level shifted and phase shifted modulation technique," *International Journal of Power Electronics and Drive Systems (IJPEDS)*, vol. 12, no. 1, Mar. 2021, doi: 10.11591/ijpeds.v12.i1.pp160-169.

[23] B. Wu and M. Narimani, *High-Power Converters and AC Drives*. Wiley, 2016, doi: 10.1002/9781119156079.

[24] A. Jewsubpong, N. Pothi, C. Rakpenthai, and J. Pahasa, "Impact of DC-link voltage ripple on induction motor drives utilizing cascaded h-bridge multilevel inverter," *ECTI Transactions on Electrical Engineering, Electronics, and Communications*, vol. 23, no. 3, 2025, doi: 10.37936/ecti-eec.2525233.259532.

[25] A. Poorfakhraei, M. Narimani, and A. Emadi, "A review of modulation and control techniques for multilevel inverters in traction applications," *IEEE Access*, vol. 9, pp. 24187–24204, 2021, doi: 10.1109/ACCESS.2021.3056612.

[26] S.-M. Yang and K.-W. Lin, "Automatic control loop tuning for permanent-magnet AC servo motor drives," *IEEE Transactions on Industrial Electronics*, vol. 63, no. 3, pp. 1499–1506, Mar. 2016, doi: 10.1109/TIE.2015.2495300.

[27] F. Mendoza-Mondragon, V. M. Hernandez-Guzman, and J. Rodriguez-Resendiz, "Robust speed control of permanent magnet synchronous motors using two-degrees-of-freedom control," *IEEE Transactions on Industrial Electronics*, vol. 65, no. 8, pp. 6099–6108, Aug. 2018, doi: 10.1109/TIE.2017.2786203.

BIOGRAPHIES OF AUTHORS



Nattapong Pothi received his B.Eng. and M.Eng. degrees in electrical engineering from Chiang Mai University, Thailand, in 2003 and 2007, respectively, and his Ph.D. in electronic and electrical engineering from the University of Sheffield, Sheffield, United Kingdom, in 2016. Since 2007, he has been with the School of Engineering at the University of Phayao, Thailand, where he is currently an assistant professor in the Department of Electrical Engineering. His research interests include electric motor drives, flux-weakening control, energy conversion systems, and power electronic applications. He can be contacted at email: nattapong.po@up.ac.th.



Buntueng Yana received his Bachelor of Engineering (B.E.) and Master of Engineering (M.E.) degrees in electrical engineering from Chiang Mai University, Thailand, in 2006 and 2009, respectively. He subsequently received his Ph.D. in information science and technology from Osaka University, Japan. Since 2010, he has been a faculty member in the Department of Electrical Engineering, School of Engineering, at the University of Phayao, Thailand, where he is currently a faculty member. His research interests include robotics, automatic control, machine learning, and biomedical image applications. He can be contacted at email: mr.buntueng@gmail.com**.**



Jonglak Pahasa received her B.Eng. degree in electrical engineering from King Mongkut's Institute of Technology Ladkrabang (KMITL), Bangkok, Thailand, in 1997; her M.Eng. degree in electrical engineering from Chiang Mai University, Chiang Mai, Thailand, in 2007; and her D.Eng. degree in electrical engineering from KMITL in 2011. She is currently an associate professor at the School of Engineering, University of Phayao, Phayao, Thailand. Her research interests include the application of artificial intelligence to power system stability and control. She can be contacted at email: jonglak.pa@up.ac.th.



Chawasak Rakpenthai received his B.Eng., M.Eng., and Ph.D. degrees in electrical engineering from Chiang Mai University, Thailand, in 1999, 2003, and 2007, respectively. He is currently a professor in the Department of Electrical Engineering at the University of Phayao, Phayao, Thailand. His research interests include applications of artificial intelligence in power systems, power electronics, power system state estimation, and flexible AC transmission system (FACTS) devices. He can be contacted at email: chawasak.ra@up.ac.th.